AN INVESTIGATION ON FLUID-STRUCTURE INTERACTION OF TWO TANDEM RECTANGULAR CYLINDERS

UDC:532.5:519.6
Original scientific paper https://doi.org/10.18485/aeletters.2023.8.4.3

Mahdi Tabatabaei Malazi[1], Muharrem Hilmi Aksoy[2*], Abdulkerim Okbaz[3,4]

[1] Department of Mechanical Engineering, Faculty of Engineering, Istanbul Aydin University, Istanbul 34295, Türkiye
[2] Department of Mechanical Engineering, Faculty of Engineering and Natural Sciences, Konya Technical University, 42020, Konya, Türkiye
[3] Department of Mechanical Engineering, Dogus University, 34775, Istanbul, Türkiye
[4] School of Materials Science and Engineering, Georgia Institute of Technology, Atlanta, GA 30332, United States

Abstract:
This paper presents a numerical investigation of the three-dimensional flow field with deformations of two tandem rectangular cylinders. The one-way Fluid-Structure Interaction (FSI) method simulated the deformation domain. The Realizable *k-ε* turbulence model was utilized to model turbulent flow simulation in the three-dimensional flow domain. The hydrodynamic forces, deformations, and stresses were calculated for different spacing configurations between the rectangular cylinders. Structural steel was chosen for the rectangular cylinders, while water was chosen for the fluid domain. The flow inlet velocity was maintained at 5 m/s for all simulations, resulting in a corresponding Reynolds number of 5×10^5 based on free stream velocity and cylinder width. The numerical results demonstrated that the cylinder spacing significantly affected the cylinders' deformation. The distance ratio between the two tandem rectangular cylinders to the cylinder height (*x/H*) was increased from 1 to 5. The front rectangular cylinder endured a higher pressure load than the rear rectangular cylinder, with the maximum deformation of the front cylinder found to be 7.15 mm. Due to the lower pressure on the rear rectangular cylinders, deformation varied between 0.98 mm and 6.02 mm as *x/H* changed from 1 to 5. This research provides valuable insights into the deformation behavior of tandem rectangular cylinders in three-dimensional flow fields.

ARTICLE HISTORY
Received: 5 June 2023
Revised: 29 October 2023
Accepted: 13 November 2023
Published: 31 December 2023

KEYWORDS
Computational Fluid Dynamics, Fluid-Structure Interaction, tandem cylinders, turbulent flow

1. INTRODUCTION

Fluid-structure interaction (FSI) is a rapidly growing field of research that has gained significant attention in recent years due to its relevance in various engineering applications. FSI is concerned with the interaction between fluid and structures, which can manifest in various forms, including the deformation of structures due to fluid forces, the flow-induced vibration of structures, and the alteration of fluid flow patterns by the presence of structures [1, 2].

In particular, the interaction between fluid and structures in the form of cylinders has become an important area of investigation in FSI due to its prevalence in numerous practical applications. Tandem cylinder systems, in which two cylinders are placed in close proximity, are of particular interest as they have been shown to exhibit complex fluid-structure interaction phenomena.

*CONTACT: M.H. Aksoy, e-mail: mhaksoy@ktun.edu.tr

Such systems are commonly found in offshore structures, heat exchangers, bridge piers, water turbines, offshore wind turbine platforms, and other applications where flow-induced vibrations and drag forces can significantly impact the overall system performance [3, 4]. Understanding the fundamental mechanisms underlying the FSI in tandem cylinder systems is crucial for the design, optimization, and safety assessment of these structures. Numerical simulations, experimental studies, and theoretical analyses have been extensively employed to investigate the complex FSI phenomena in tandem cylinder systems. These efforts have led to significant advances in understanding the interaction between fluid and cylinders and have provided valuable insights into the underlying physical mechanisms governing the FSI phenomena [5].

Numerical simulation methods have become prevalent in investigating physical and mechanical problems in various engineering applications. In fluid mechanics, numerical studies have been extensively conducted on the interaction between contiguous rigid bodies and fluid flows. In this regard, several notable studies have been summarized in this section. Tabatabaei Malazi et al. [6] conducted an experimental and numerical investigation of three-dimensional T-shaped flexible cylinder deformation using a high-speed camera system and a two-way FSI numerical method. The tree models' drag force, deformation, and stress were evaluated using CFD techniques across various wind velocities and geometric factors by Amani-Beni et al. [7]. The deformation of the tree was solved using the one-way FSI approach. The findings suggest that wind velocity and the tree's geometric characteristics significantly influence a tree's deformation, drag force, and stress.

In another article, the treatment of local scour around three adjacent piles by simulating the flow field around them was studied. The simulation predicted the sediment motion regarding its advection, erosion, and deposition. Moreover, studies investigated the impact of pile spacing and arrangement on flow fields, bed elevation contours, and scour depth [8]. In previous studies, vegetation was often modelled as rigid cylinders, but concerns were raised about the accuracy of such models in replicating the effects of actual vegetation. A numerical simulation assessed the consequences of representing plants as rigid cylinders. The findings showed that the flow resistance decreases with the Reynolds number for rigid cylinders and plants.

Furthermore, the Baptist method, which estimates the impact of vegetation drag and bed shear stress, underestimated bed erosion within sparse vegetation in rivers and overestimated the mean flow velocity [9]. In another study, equations governing fluid flows in vegetated areas were derived, assuming vegetation to be straight and rigid cylinders. The presence of vegetation significantly affected the dissipation of flow energy inside and outside the vegetation in the wake flow region [10].

Additionally, a 3D simulation was conducted to investigate flow and scour/backfilling around a pile exposed to waves based on Reynolds-averaged Navier-Stokes equations, analyzing two types of beds: sediment bed and rigid bed. For the rigid-bed case, it was discovered that vortex shedding for waves around the pile occurs in a "one-cell" manner with a uniform shedding frequency, unlike in a steady current where a two-cell structure prevails [11]. In nuclear reactors, arrays of cylinders are frequently employed as heat exchangers. Large-eddy simulations examined a single rigid cylinder representative of a cylinder in an infinite square array on a numerical domain, analyzing its spacing and effect on wall pressure [12]. The relationship between the state and resistance of submerged vegetation and its relative bending rigidity was also determined by studying the submerged vegetation's state under various inflow conditions [13]. The variation of drag coefficient in subcritical open channels was also examined for rigid vegetation by Liu et al. [14]. Finally, artificial, tree-like emergent vegetation elements with a relatively simple structure were used to experimentally investigate channel flow through tree-like vegetation, evaluating the canopy's impact on the flow field. The findings indicate that canopy porosity significantly affects the sub-canopy flow intensity [15].

Several studies have explored the effects of different parameters on the FSI of multiple cylinders, such as spacing ratio, arrangement pattern, Reynolds number, mass ratio, damping ratio, etc. [16] Other notable studies in this area include the investigation of emergent blade-type vegetation stems [17] and floating wind turbines [18]. The present work examines the FSI characteristics of two rectangular cylinders arranged in tandem through numerical simulations. The deformation, hydrodynamic forces, and stresses of the cylinders were analyzed for different cylinder spacing.

The primary objective of this study is to conduct a numerical investigation into the FSI of two tandem rectangular cylinders in a complex three-dimensional flow field. Leveraging advanced CFD techniques, including the Realizable k-ε turbulence model and the one-way FSI method, the research explores hydrodynamic forces, deformations, stresses, and drag coefficients. The aim is to provide invaluable insights into the behavior of these tandem structures under varying FSI conditions, expressed as different *x/H* ratios. This investigation significantly contributes to the understanding of fluid-structure interaction phenomena, offering essential knowledge for the design, optimization, and safety evaluation of similar systems in diverse engineering applications.

2. METHODS

2.1 Computational Model, Boundary Conditions, and Meshing

Simulations were utilized at the same velocity for various spacing. To have a better and more practical understanding, the computational domain, boundary conditions, and rectangular cylinder locations are depicted in Figs. 1 and 2.

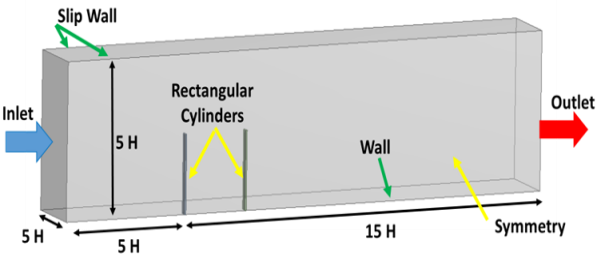

Fig. 1. Details of the computational domain

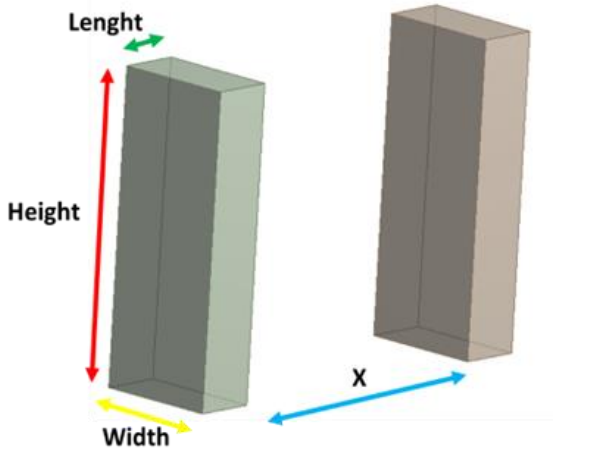

Fig. 2. Sketch view of rectangular cylinders

Dimensions and rectangular cylinder size are presented in Table 1 to specify the cylinders' height, length, width, and various tested distances. Velocity inlet, pressure outlet, slip walls, no-slip wall for rigid bed, and symmetry boundary conditions were applied in this research, as shown in Fig. 1.

Table 1. Dimensions of the rectangular cylinders in the computational domain

Height (*H*)	0.5 m
Length (*L*)	0.01 m
Width (*W*)	0.1 m
Distance between cylinders (*x/H*)	1, 2, 3, 4, 5

Mesh independence studies are commonly conducted to investigate the sensitivity of the solution to the mesh elements, numbers, and sizes to obtain accurate numerical results. This research tested various mesh configurations to obtain an independent mesh solution. Specifically, the flow domain was discretized using 3.2×10^5 tetrahedron mesh elements with prism layers over walls, while the solid domain was discretized using quad meshes with a size of 0.2 mm. The quality and distribution of the mesh elements in both the fluid and solid domains are depicted in Figs. 3-a, b, and c, respectively. These figures demonstrate the adequacy of the mesh in capturing the complex flow and solid structures in the simulation. It is worth noting that the choice of mesh elements and sizes is critical in achieving accurate and reliable numerical solutions to fluid-structure interaction problems. Therefore, the mesh independence study provides valuable insight into the appropriate mesh configurations to save computation time [19].

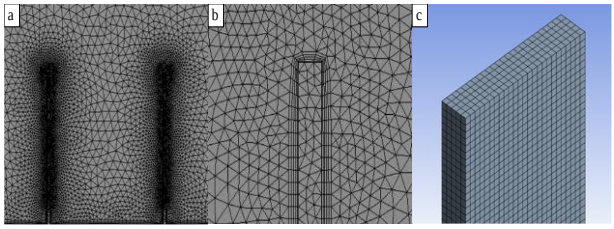

Fig. 3. a) Computational mesh of the fluid domain, b) enlarged view of the mesh, and c) mesh of the solid domain

Water was chosen as the fluid to simulate the current problem, and structural steel was selected as the solid material for the rectangular cylinders. The pertinent physical properties of these materials are listed in Table 2.

Table 2. Physical properties of the fluid and solid

Water	
Density	998.2 kg/m^3
Dynamic viscosity	0.001003 Pa·s
Structural Steel	
Density	7850 kg/m^3
Young's modulus	2x10^{11} Pa
Poisson's ratio	0.3

2.2. Computational Fluid Dynamics Simulations

This research used two commercial software packages, Ansys-Fluent and Static Structural, for the simulations. The Realizable *k-ε* turbulence model was applied to simulate steady-state turbulent flow for the three-dimensional fluid domain. The continuity and momentum equations were utilized in the simulations. These equations are presented in reference to expressions 1 and 2 [20, 21].

$$\frac{\partial \rho}{\partial t} + \frac{\partial (\rho u_i)}{\partial x_i} = 0 \quad (1)$$

$$\frac{\partial (\rho u_i)}{\partial t} + \frac{\partial (\rho u_i u_j)}{\partial x_j} = -\frac{\partial P}{\partial x_i} + \rho g_i + \frac{\partial}{\partial x_j}(\mu + \mu_t)\left(\frac{\partial u_i}{\partial x_j} + \frac{\partial u_j}{\partial x_i}\right) + S_i \quad (2)$$

Where ρ is the fluid density, $u_{i,}$ and u_j denote the average velocity components of the fluid, P represents pressure, S_i represents the momentum equation's source term, μ represents the dynamic viscosity, μ_t represents the eddy viscosity, which is calculated as $\mu_t = \rho C_\mu \frac{k^2}{\varepsilon}$, and ε is the turbulent dissipation rate. The transport equations for *k* and ε for the realizable k-ε model can be expressed as [22-24]:

$$\frac{\partial}{\partial t}(\rho k) + \frac{\partial}{\partial x_i}(\rho k u_j) = \frac{\partial}{\partial x_j}\left[\left(\mu + \frac{\mu_t}{\sigma_k}\right)\frac{\partial k}{\partial x_j}\right] + G_k - \rho\varepsilon + S_k \quad (3)$$

$$\frac{\partial}{\partial x_j}(\rho \varepsilon u_j) = \frac{\partial}{\partial x_j}\left[\left(\mu + \frac{\mu_t}{\sigma_\varepsilon}\right)\frac{\partial \varepsilon}{\partial x_j}\right] + \rho C_1 S_\varepsilon - \rho C_2 \frac{\varepsilon^2}{k + \sqrt{\upsilon \varepsilon}} + S_\varepsilon \quad (4)$$

Where,

$$C_1 = \max\left[0.43, \frac{\eta}{\eta + 5}\right], \eta = S\frac{k}{\varepsilon}, S = \sqrt{2 S_{ij} S_{ij}} \quad (5)$$

In the equations, *k* represents the turbulent kinetic energy. *ε* represents the rate of dissipation. G_k is turbulent kinetic energy generation, G_b is turbulent kinetic energy generation, and Y_M is fluctuating dilatation contribution to the overall dissipation rate. The model constants for the realizable *k-ε* turbulence model can be written as $C_{1\varepsilon} = 1.44$, $C_{2\varepsilon} = 1.92$, $\sigma_k = 1.0$, $C_\mu = 0.09$, and $\sigma_\varepsilon = 1.3$.

This research employed the SIMPLE algorithm to couple the continuity and momentum equations to solve the problem. The solution was deemed acceptable when the residuals of the x-velocity, y-velocity, and z-velocity equations were reduced below 10^{-6}.

The Reynolds number in this research was 5×10^5, as defined in Eq. (6). The free-stream velocity (U_∞) was set to 5 m/s, the characteristic length of the cylinder was 0.1 m, and the kinematic viscosity of water was represented by ν.

$$Re = \frac{U_\infty D}{\upsilon} \quad (6)$$

2.3. Computational Structural Dynamics Simulations

The deformation of a three-dimensional flexible solid structure can be mathematically described by Equation (7) [25].

$$[M]\{\ddot{u}\} + [C]\{\dot{u}\} + [K]\{u\} = \{F\} \quad (7)$$

Here, *[M]* represents the mass matrix of the structure, [C] represents the damping matrix, *[K]* represents the stiffness matrix, and *{F}* represents the load vector acting on the solid structure due to fluid. The nodal acceleration vector is denoted by $\{\ddot{u}\}$, the nodal velocity vector by $\{\dot{u}\}$, and the nodal displacement vector by {u}. The Equation provides a comprehensive representation of the dynamic behavior of the solid structure in response to the fluid forces acting on it.

Total deformation was computed numerically in a three-dimensional flexible solid structure by expression (8).

$$U = \sqrt{U_x^2 + U_y^2 + U_z^2} \quad (8)$$

where U_x, U_y, and U_z are component deformations in the x, y, and z directions, respectively.

The Von Mises stress in a three-dimensional flexible solid structure can be numerically calculated using Equation (9).

$$\sigma_e = \left[\frac{(\sigma_1 - \sigma_2)^2 + (\sigma_2 - \sigma_3)^2 + (\sigma_3 - \sigma_1)^2}{2}\right]^{\frac{1}{2}} \quad (9)$$

where σ_1, σ_2 and σ_3 are stress states in the *x*, *y*, and *z* directions, respectively.

3. RESULTS AND DISCUSSIONS

As a preamble to the fluid flow effect, the results of the pressure produced by the water acting on the front surfaces of rectangular cylinders are discussed and given in Fig. 4. The pressure distribution on the front surface of the rectangular cylinders against water flow is shown for both the front (the left figure) and rear sides (the right figure), where the *x/H* was changed from 1 to 5. From the obtained results in low *x/H* (in which rectangular cylinders were close to each other), the rear rectangular cylinder was not exposed to direct flow, and pressure levels were low. However, as *x/H* increased, the rear rectangular cylinder experienced a substantial increase in force, accompanied by a rise in pressure levels, as illustrated in the contours. As a result of the front rectangular cylinder being a bluff body, it caused a massive flow separation, and a large wake was formed. Therefore, the pressure effect on the rear rectangular cylinder changed with distance, and the pressure force was low on the rear cylinder when the cylinders were close to each other. Moreover, owing to the flow separation occurring on the upper side of the front rectangular cylinder, the rear rectangular cylinder endured substantial forces. The pressure distribution of the rear rectangular cylinder illustrates that pressure increased from bottom to top on the front surface of the rear rectangular cylinder.

3.1. Flow Structure Results

Fig. 5 (a) shows the velocity vector distribution of the single rectangular cylinder and (b) the symmetry plane when the tandem arrangement was *x/H* = 1. The velocity was high at the edges of the front rectangular cylinder, and the velocity distribution on the rear rectangular cylinder shows that the velocity value was also high in the central region of the rectangular cylinder. Hence, the front rectangular cylinder caused flow recirculation near the rear rectangular cylinder. In addition, velocity vectors indicate how the fluid motion in different positions changed. The fluid velocity decreased to its lowest (approximately zero) when hitting the rectangular cylinder as an obstacle in the flow direction. On the other hand, vortex formation can be observed in the region between two cylinders. Also, the flow separation generated recirculation zones at the rear side of the cylinder visible.

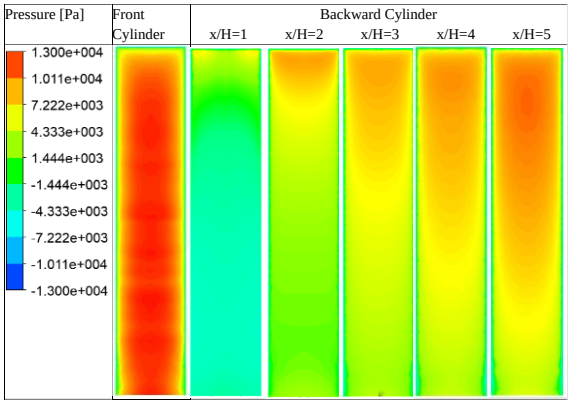

Fig. 4. The pressure contours at the front and rear side of the cylinders for different *x/H*

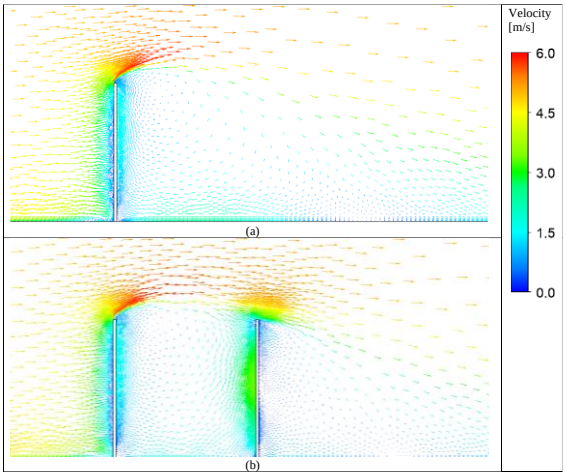

Fig. 5. Velocity vectors around rectangular cylinders. a) Single cylinder and b) tandem cylinders at *x/H*=1

3.2. Deformation and Stress Results

The maximum deformation of the rear cylinder was recorded at different *x/H* values from 1 to 5 and demonstrated in Fig. 6. The maximum deformation value was 7.15 mm for the front rectangular cylinder. The lowest deformation was obtained at 0.92 mm, while the highest was 6.1 mm for the rear rectangular cylinders. The results indicated that the deformation value initially increased with a high slope. Subsequently, the rate of increase gradually diminished, and the curve ascended until it reached its peak, matching that of the front cylinder. It was realized that the front rectangular cylinder had a lower effect on the rear rectangular cylinder when the distance between rectangular cylinders increased.

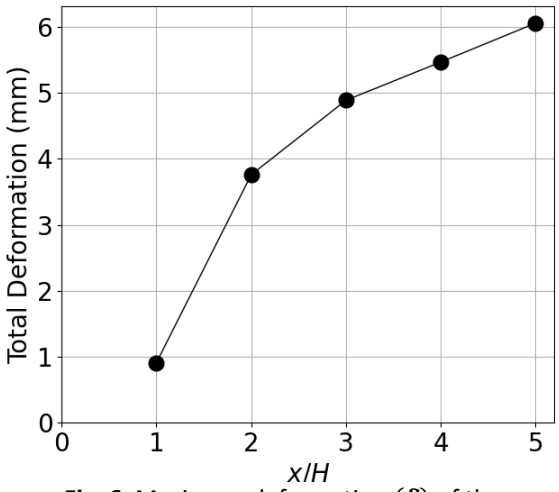

Fig. 6. Maximum deformation (δ) of the rear rectangular cylinder at various *x/H*

Fig. 7 shows the Von Mises maximum stress at different *x/H*. It has a similar trend with the deformation values. It was demonstrated that the Von Mises maximum stress increased when the distance between rectangular cylinders expanded because of the heightened pressure force on the rear rectangular cylinder. The results show that the value of the Von Mises maximum was 123 MPa for the front rectangular cylinder. The value of the Von Mises maximum stress was changed from 10.8 MPa to 102 MPa when the value of *x/H* was changed from 1 to 5.

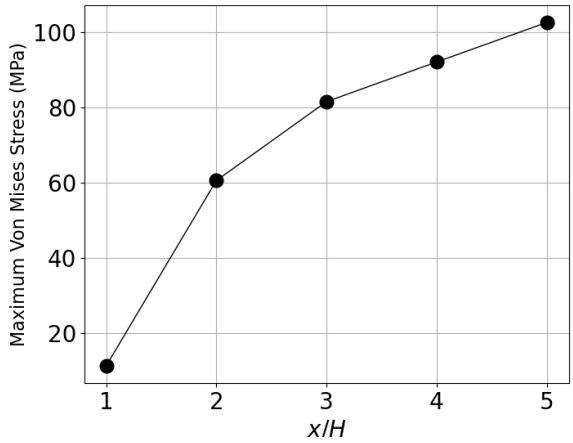

Fig. 7. The Von Mises maximum stress of the rear rectangular cylinder at various *x/H*

In the Figs. 8 and 9, rectangular cylinder deformation is compared to the front and rear rectangular cylinders when the *x/H* is 5. The front cylinder experienced a greater pressure load and endured the highest force exerted by the fluid flow. The front cylinder experienced higher pressure, resulting in a maximum deformation of 7.15 mm, while the other cylinder, subject to lower pressure, exhibited a maximum deformation of about 6.02 mm.

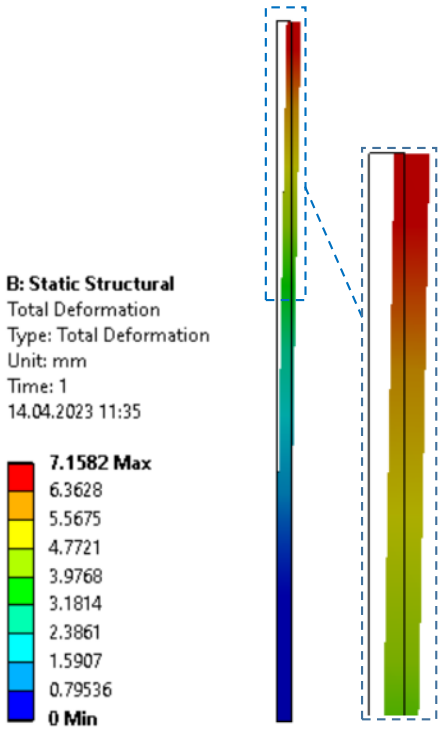

a)

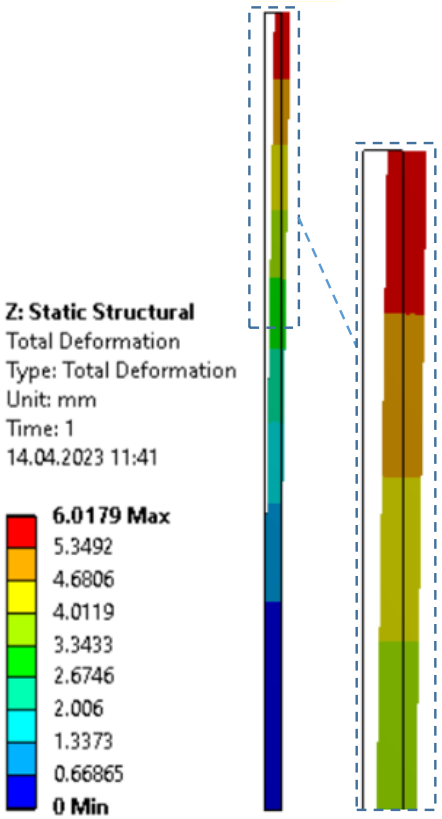

b)

Fig. 8. The deformation of a) the front rectangular cylinder and b) the rear rectangular cylinder at *x/H* =5 at V= 5 m/s

3.3. Drag Coefficients Results

A drag force is exerted on an object when it is placed in a fluid flow. The drag force on a rectangular cylinder during water flow can be calculated using Equation (10).

$$F_D = F_{D_p} + F_{D_v} = \oint P\,\hat{n}\,.\,\hat{e}_d dS + \oint \tau_w\,\hat{t}\,.\,\hat{e}_d dS \quad (10)$$

where, F_{D_p} is pressure drag, F_{D_v} is viscous drag, p is the pressure, and τ is the wall shear stress. After calculating the force of drag, the drag coefficient can be calculated using Equation. (11).

$$C_D = \frac{F_D}{\frac{1}{2}\rho U^2 A} \quad (11)$$

Where C_D is the drag coefficient, F_D is the total drag force, ρ is the density of the fluid, U is the velocity of the fluid, and A is the characteristic area of the body (rectangular cylinder frontal area).

Figure 9 shows the variation of the total force with *x/H*. The front rectangular cylinder had a total drag force of approximately 772. The value of the minimum drag force for the rear rectangular cylinder was 2.62 N when *x/H* was 1. On the other hand, it was 610 N when *x/H* was 5. It was determined that the total drag force of the rear rectangular cylinder increased with increasing distance between the rectangular cylinders.

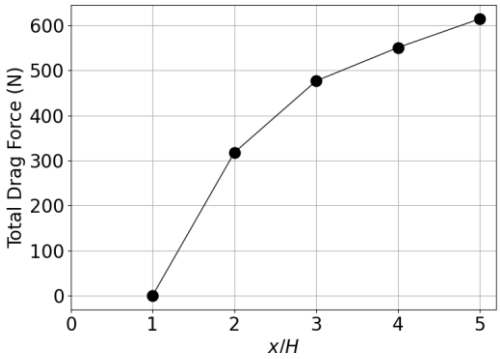

Fig. 9. The total drag force of the rear cylinder varies with *x/H*

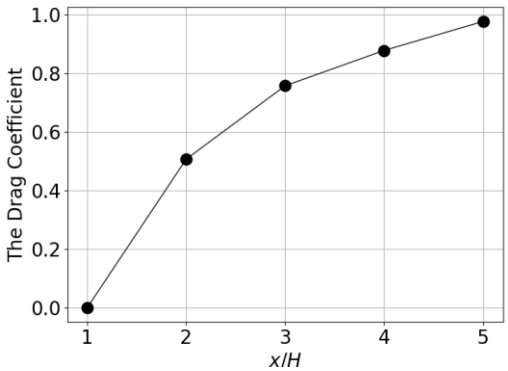

Fig. 10. The drag coefficients of the rear cylinder vary with *x/H*

As can be seen from Figure 10, the drag coefficient increased as the distance between the cylinders increased. The drag coefficient of the front rectangular cylinder is nearly 1.23. When *x/H* was 1, the rear rectangular cylinder's minimum drag coefficient was measured as 0.0041. On the other side, when *x/H* was 5, it was 0.97. It is seen that the front cylinder absorbed some of the momentum coming to the rear cylinder and reduced the drag force.

4. CONCLUSIONS

The findings of this study have practical implications in several engineering applications. They are invaluable for designing stable offshore structures, optimizing heat exchanger systems, constructing resilient bridges and buildings in challenging environments, enhancing the efficiency of water turbines in hydropower plants, improving aerodynamic designs in aerospace and automotive industries, and ensuring the durability of renewable energy devices like tidal turbines and wind turbines. Understanding fluid-structure interaction is essential for engineering designs across these diverse applications, ensuring they are efficient, durable, and capable of withstanding complex environmental forces.

The present research demonstrates the utility of numerical simulations for investigating FSI in complex geometries and flow conditions. This research focuses on the tandem cylinder system, an important aspect of FSI that significantly affects system behavior. The simulations employ the one-way FSI method and the Realizable k-ε turbulence model for the three-dimensional flow domain.

The numerical results revealed that the deformation, pressure force, and stress depend on the distance between rectangular cylinders. When the cylinders were positioned close together (low *x*/*H* values), the front cylinder created significant flow separation, causing low pressure and drag forces on the rear cylinder. As the distance between the cylinders increased (high *x*/*H* values), the influence of the front cylinder's flow separation decreased, resulting in higher pressure and drag forces on the rear cylinder. This phenomenon resulted in variations in deformation, stress, and drag coefficients. The total drag force was almost 99% lower on the rear rectangular cylinder for *x/H* = 1 than at the front rectangular cylinder. In addition, the total drag force on the rear rectangular cylinder was nearly 21% smaller when x/*H* was 5, compared to that on the front rectangular cylinder.

The research also shows that the rear rectangular cylinder experienced almost 87% less maximum deformation than the front rectangular cylinder at *x/H* = 1. Moreover, at *x/H* of 5, the maximum deformation was reduced by nearly 16% at the rear rectangular cylinder compared to the front rectangular cylinder.

The insights gained from this research can be instrumental in designing structures subjected to FSI, resulting in more efficient and reliable engineering designs. Studying diverse geometric shapes, mainly circular or elliptical cross-sections, can shed light on their impact on deformation and pressure distribution. Unraveling turbulent flow complexities and expanding investigations to configurations with more than two cylinders, exploring the influence of surface roughness on boundary layer formation and drag forces holds promise. Implementing coupled fluid-structure optimization algorithms and integrating experimental techniques like Particle Image Velocimetry (PIV) can enhance accuracy.

REFERENCES

[1] H. Gotoh, A.Khayyer, Y. Shimizu, Entirely Lagrangian meshfree computational methods for hydroelastic fluid-structure interactions in ocean engineering-Reliability, adaptivity and generality. *Applied Ocean Research*, 115, 2021: 102822. https://doi.org/10.1016/j.apor.2021.102822

[2] D.T. Yaseen, M.A. Ismael, Analysis of power law fluid-structure interaction in an open trapezoidal cavity. *International Journal of Mechanical Sciences*, 174, 2020: 105481. https://doi.org/10.1016/j.ijmecsci.2020.105481

[3] U. Ali, M. Islam, I. Janajreh, Y. Fatt, M.M. Alam, Flow-induced vibrations of single and multiple heated circular cylinders: A review. *Energies*, 14(24), 2021: 8496. https://doi.org/10.3390/en14248496

[4] I. Goktepeli, U. Atmaca, A. Cakan, Investigation of heat transfer augmentation between the ribbed plates via Taguchi approach and computational fluid dynamics. *Journal of Thermal Science*, 29, 2020: 647-666. https://doi.org/10.1007/s11630-019-1155-z

[5] C. Zong, Q. Li, K. Li, X. Song, D. Chen, X. Li, X. Wang, Computational fluid dynamics analysis and extended adaptive hybrid functions model-based design optimization of an explosion-proof safety valve. *Engineering Applications of Computational Fluid Mechanics*, 16(1), 2022: 296-315. https://doi.org/10.1080/19942060.2021.2010602

[6] M. Tabatabaei Malazi, E.T. Eren, J. Luo, S. Mi, G. Temir, Three-dimensional fluid-structure interaction case study on elastic beam. *Journal of Marine Science and Engineering*, 8(9), 2020: 714. https://doi.org/10.3390/JMSE8090714

[7] M. Amani-Beni, M. Tabatabaei Malazi, K. Dehghanian, L. Dehghanifarsani, Investigating the effects of wind loading on three dimensional tree models using numerical simulation with implications for urban design. *Scientific Reports*, 13, 2023: 7277. https://doi.org/10.1038/s41598-023-34071-5

[8] Q. Zhang, X.-L. Zhou, J.-H. Wang, Numerical investigation of local scour around three adjacent piles with different arrangements under current. *Ocean Engineering*, 142, 2017: 625-638. https://doi.org/10.1016/J.OCEANENG.2017.07.045

[9] A. Vargas-Luna, A. Crosato, G. Calvani, W.S.J. Uijttewaal, Representing plants as rigid cylinders in experiments and models. *Advances in Water Resources*, 93, 2016: 205-222. https://doi.org/10.1016/J.ADVWATRES.2015.10.004

[10] J.-t. Zhang, X.-h. Su, Numerical model for flow motion with vegetation. *Journal of Hydrodynamics*, 20, 2008: 172-178. https://doi.org/10.1016/S1001-6058(08)60043-8

[11] C. Baykal, B.M. Sumer, D.R. Fuhrman, N.G. Jacobsen, J. Fredsøe, Numerical simulation of scour and backfilling processes around a circular pile in waves. *Coastal Engineering*, 122, 2017: 87-107. https://doi.org/10.1016/J.COASTALENG.2017.01.004

[12] L. De Moerloose, P. Aerts, J. De Ridder, J. Vierendeels, J. Degroote, Numerical investigation of large-scale vortices in an array of cylinders in axial flow. *Journal of Fluids and Structures*, 78, 2018: 277-298. https://doi.org/10.1016/J.JFLUIDSTRUCTS.2018.01.002

[13] L.-h. Wu, X.-l. Yang, Influence of bending rigidity of submerged vegetation on local flow resistance. *Journal of Hydrodynamics*, 26, 2014: 242-249.

https://doi.org/10.1016/S1001-6058(14)60027-5

[14] X.-g. Liu, Y.-h. Zeng, Drag Coefficient for Rigid Vegetation in Subcritical Open Channel. *Procedia Engineering*, 154, 2016: 1124-1131. https://doi.org/10.1016/J.PROENG.2016.07.522

[15] V. Kitsikoudis, O. Yagci, V.S.O. Kirca, D. Kellecioglu, Experimental investigation of channel flow through idealized isolated tree-like vegetation. *Environmental Fluid Mechanics*, 16, 2016: 1283-1308. https://doi.org/10.1007/s10652-016-9487-7

[16] Z.G. Liu, Y. Liu, J. Lu, Fluid-structure interaction of single flexible cylinder in axial flow. *Computers & Fluids*, 56, 2012: 143-151. https://doi.org/10.1016/j.compfluid.2011.12.003

[17] A.O. Busari, C.W. Li, Bulk drag of a regular array of emergent blade-type vegetation stems under gradually varied flow. *Journal of Hydro-environment Research*, 12, 2016: 59-69. https://doi.org/10.1016/J.JHER.2016.02.003

[18] S. Rockel, J. Peinke, M. Hölling, R.B. Cal, Wake to wake interaction of floating wind turbine models in free pitch motion: An eddy viscosity and mixing length approach. *Renewable Energy*, 85, 2016: 666-676. https://doi.org/10.1016/J.RENENE.2015.07.012

[19] O. Babayigit, M. Ozgoren, M.H. Aksoy, O. Kocaaslan, Experimental and CFD investigation of a multistage centrifugal pump including leakages and balance holes. Desalination and Water Treatment, 67(3), 2017: 28-40. https://doi.org/10.5004/dwt.2017.20153

[20] E. Canli, A. Ateş, Ş. Bilir, Derivation of dimensionless governing equations for axisymmetric incompressible turbulent flow heat transfer based on standard k-ϵ model. *Afyon Kocatepe Üniversitesi Fen Ve Mühendislik Bilimleri Dergisi*, 20(6), 2020: 1096-1111. https://doi.org/10.35414/akufemubid.821009

[21] E. Canli, A. Ateş, Ş. Bilir, Developing turbulent flow in pipes and analysis of entrance region. *Academic Platform-Journal of Engineering and Science*, 9(2), 2021: 332-353. https://doi.org/10.21541/apjes.818717

[22] S. Yagmur, S. Dogan, M.H. Aksoy, I. Goktepeli, Turbulence modeling approaches on unsteady flow structures around a semi-circular cylinder. *Ocean Engineering*, 200, 2020: 107051. https://doi.org/10.1016/j.oceaneng.2020.107051

[23] M.H. Aksoy, S. Yagmur, S. Dogan, CFD Modelling of Industrial Air Curtains with Heating Unit. *EPJ Web of Conferences EDP Sciences*, 213, 2019: 02001. https://doi.org/10.1051/epjconf/201921302001

[24] ANSYS Fluent Theory Guide. *ANSYS Inc.*, Canonsburg, USA, 2017, 724-746.

[25] A.B. Olcay, M. Tabatabaei Malazi, The effects of a longfin inshore squid's fins on propulsive efficiency during underwater swimming. *Ocean Engineering*, 128, 2016: 173-182. https://doi.org/10.1016/j.oceaneng.2016.10.037